

Secondary bias of dark matter halos: Perspective in the linear density field

Xiaoyu Wang^{1,2}, Huiyuan Wang^{1,2}, H.J. Mo³, JingJing Shi⁴, Yipeng Jing^{5,1}

¹ Key Laboratory for Research in Galaxies and Cosmology, Department of Astronomy, University of Science and Technology of China, Hefei, Anhui 230026, China; wambyybz@mail.ustc.edu.cn, whywang@ustc.edu.cn

² School of Astronomy and Space Science, University of Science and Technology of China, Hefei 230026, China

³ Department of Astronomy, University of Massachusetts, Amherst MA 01003-9305, USA

⁴ Institute for the Physics and Mathematics of the Universe (Kavli IPMU, WPI), UTIAS, Tokyo Institutes for Advanced Study, University of Tokyo, Chiba, 277-8583, Japan

⁵ Department of Astronomy, and IFSA Collaborative Innovation Center, Shanghai Jiao Tong University, Shanghai 200240, China

April 30, 2022

ABSTRACT

Using two sets of large N -body simulations, we study the origin of the correlations of halo assembly time (z_f), concentration (v_{\max}/v_{200}) and spin (λ) with the large-scale density field around halos. We find that the correlations of the three halo properties with the large-scale density at $z = 0$ are the secondary effects of their correlations with the initial linear density field. Using the linear density on different scales, we find two types of correlations. The L -correlation, which describes the correlation of halo properties with the mean linear over-density δ_L^i within the halo Lagrangian radius R_L , is positive for both z_f and v_{\max}/v_{200} , and negative for λ . The E -correlation, which describes the correlations of halo properties with $\delta^i(R/R_L > 1)$ for given δ_L^i , shows trends opposite to the L -correlation. Both of the E - and L -correlations depend only weakly on halo mass, indicating a similar origin for halos of different masses. The dependence of the halo bias on the three halo properties can be well explained by the competition of the E - and L -correlations and the correlation of the linear density field on different scales. These two types of correlation together can establish the complex halo-mass dependence of the clustering bias produced by the three halo properties.

Key words. large-scale structure of Universe – dark matter – methods: N -body simulations – methods: statistical

1. Introduction

Numerical N -body simulations have revealed that the clustering of dark matter halos depends not only on halo mass (e.g. Mo & White 1996; Sheth et al. 2001) but also on other halo properties, such as mass assembly history, and structural and dynamical properties (Gao et al. 2005; Wechsler et al. 2006; Wetzel et al. 2007; Jing et al. 2007; Bett et al. 2007; Gao & White 2007; Li et al. 2008; Faltenbacher & White 2010; Lacerna & Padilla 2011; Lazeyras et al. 2017; Xu & Zheng 2018; Salcedo et al. 2018; Mao et al. 2018; Chue et al. 2018). The dependence of the halo clustering on the halo properties other than halo mass is usually referred to as the halo assembly bias or the secondary bias. Understanding the secondary bias is important for understanding the formation of dark matter halos in the cosmic density field, as well as for understanding galaxy formation and evolution in dark matter halos (see e.g. Zhu et al. 2006; Yang et al. 2006; Zentner et al. 2014; Hearin et al. 2015; Wechsler & Tinker 2018; Wang et al. 2018; Salcedo et al. 2020).

It is well known that halo properties, such as the assembly time, concentration, substructure and spin, are correlated among themselves (e.g. Jing & Suto 2002; Zhao et al. 2003; Gao et al. 2004; Allgood et al. 2006; Hahn et al. 2007; Wang et al. 2011; Mao et al. 2018). However, these proper-

ties exhibit complex trends in their secondary bias, sometimes in a way different from that expected from their mutual correlations. For instance, the dependence of the halo clustering on the assembly time is usually strong for low-mass halos, but weak at the massive end (see e.g. Gao et al. 2005; Jing et al. 2007; Li et al. 2008; Mao et al. 2018; Chue et al. 2018), while the secondary bias for the halo spin parameter increases with halo mass (e.g. Bett et al. 2007; Gao & White 2007; Faltenbacher & White 2010; Salcedo et al. 2018). Moreover, the dependence of the secondary bias on the two halo structural parameters, halo concentration and subhalo abundance, changes sign at around the characteristic mass of collapse (Wechsler et al. 2006; Gao & White 2007; Salcedo et al. 2018).

These results imply that the secondary bias has multiple origins. This is supported by many investigations in the literature, most of which focused on the secondary bias of the assembly time. For example, Wang et al. (2007) found that old small halos are usually located closer to massive structures than their young counterparts (see also Hahn et al. 2009), a phenomenon referred to as the neighbour bias by Salcedo et al. (2018). Further studies showed that the secondary bias may also be related to the nearby cosmic web of halos (Yang et al. 2017; Paranjape et al. 2018; Ramakrishnan et al. 2019). Several processes related to the presence of massive neighbours have been proposed. For instance,

the tidal field of the massive structure can accelerate the ambient matter and truncate the mass accretion onto small halos (Wang et al. 2007; Hahn et al. 2009; Wang et al. 2011; Shi et al. 2015; Paranjape et al. 2018; Mansfield & Kravtsov 2020). Splashback halos that have ever passed through massive host halos may be severely stripped by the tidal force of the hosts (Ludlow et al. 2009; Wang et al. 2009). These halos with close massive companions are expected to have an early assembly time because of the truncation of late accretion, and can contribute significantly to the secondary bias (Wang et al. 2009; Li et al. 2013; Mansfield & Kravtsov 2020; Tucci et al. 2020).

In addition to the truncation and stripping processes, Wang et al. (2011) found that dense environments can also enhance mass accretion by halos (see also Fakhouri & Ma 2009). This process is expected to yield a trend in the halo bias with assembly time that is different from the measured secondary bias. These authors suggested that the halo-mass dependence of the secondary bias is partly caused by the competition between two categories of processes, the truncation by large-scale tidal field and the availability of material to be accreted by halos (see also Chen et al. 2020). However, exactly how these processes contribute to the secondary bias is still unclear.

Suggestions have been made that the secondary bias in halo concentration may share a common origin with the secondary bias in the assembly time (Han et al. 2019; Chen et al. 2020), although the two properties exhibit different trends as discussed above. Several studies (Salcedo et al. 2018; Han et al. 2019; Johnson et al. 2019; Tucci et al. 2020) pointed out that the secondary bias for the spin may have a different origin than both the assembly time and concentration. The correlation and alignment of the spin amplitude and direction with the local tidal field suggest that the tidal torques may play a key role in establishing the dependence of halo bias on spin (Hahn et al. 2007; Shi et al. 2015; Chen et al. 2016; Wang & Kang 2018). Unfortunately, it is still unclear how the secondary bias for the concentration and spin is established and whether it is related to halo assembly or it is produced by completely different processes.

Attempts have also been made to understand the origin of the secondary bias from the initial conditions (e.g. Wang et al. 2007; Zentner 2007; Sandvik et al. 2007; Dalal et al. 2008; Desjacques 2008; Musso & Sheth 2012; Shi & Sheth 2018). For example, Wang et al. (2007) found that low-mass, older halos tend to be associated with perturbations of higher mass in the initial density field (the initial mass) that are expected to collapse into halos according to the spherical collapse model. They further found that the bias relation obtained from the initial masses in N -body simulations actually matches the secondary bias of the assembly time. Dalal et al. (2008) used the properties of density peaks in the initial conditions to infer the halo assembly time and concentration, and found that the general trends in the secondary bias of these two halo properties can be reproduced in their model. For massive halos, they suggested that the secondary bias reflects the statistics of the random Gaussian field (see also Zentner 2007), while for low-mass halos, they reached conclusions that are similar to those in earlier studies (e.g. Wang et al. 2007, 2009). More recently using the excursion set approach, Shi & Sheth (2018) suggested that the secondary bias possibly reflects the correlation of densities at different scales when the density at the halo-

mass scale is fixed. All these results provide valuable insight into the origin of the secondary bias. However, the correlations between peak properties and halo properties are ambiguous, and the excursion set approach is not able to model the effects of tidal truncation.

Thus, the details of the secondary bias, in particular its mass dependence, remain unresolved. It is still unclear whether or not the secondary bias for low- and high-mass halos have the same origins. It is also unclear why different halo properties exhibit different trend in their secondary bias, although they are correlated. Furthermore, since the secondary bias may already be present in the initial conditions, it is important to understand how it is connected to the secondary bias observed for the halo population in the evolved density field, and whether the initial condition or later evolution plays the more important role in determining the secondary bias.

In this paper, we use both the evolved density field (at $z = 0$) and the linear density field to study the secondary bias of three halo properties: assembly time, concentration and spin. We use various correlation analyses to disentangle different effects. The paper is organized as follows. In Section 2, we describe the simulations, dark matter halo samples, merger tree construction, and the quantities we use for our analyses. In section 3, we study the correlations of halo properties with evolved and linear densities at a typical large scale where halo bias can be measured. In Section 4, we study the correlations of halo properties with linear densities at various scales and present our findings of two types of correlations that can affect the secondary bias of halos. In Section 5, we use the two types of correlations to interpret the secondary bias for different halo properties and its dependence on halo mass. Finally, we summarize and discuss our results in Section 6.

2. Simulations and Dark Matter Halos

2.1. Simulations, Halos and Merger trees

Two simulations with different mass resolution are used in this paper. The higher resolution one is the ELUCID simulation carried out by Wang et al. (2016) using L-GADGET code, a memory-optimized version of GADGET-2 (Springel 2005). This simulation has 3072^3 dark matter particles, each with a mass of $3.08 \times 10^8 h^{-1} M_\odot$, in a periodic cubic box of 500 comoving $h^{-1} \text{Mpc}$ on a side. The other simulation has 2048^3 particles in a cubic box of $1 h^{-1} \text{Gpc}$ on a side, with particle mass of $8.3 \times 10^9 h^{-1} M_\odot$. This simulation is referred to as S1k in the following. The initial conditions of the two simulations are generated at redshift of 100 by using the Zel'dovich approximation (Zel'Dovich 1970). The cosmology parameters used in the simulations are both based on WMAP5 (Dunkley et al. 2009): $\Omega_{\Lambda,0} = 0.742$, $\Omega_{m,0} = 0.258$, $\Omega_{b,0} = 0.044$, $h = H_0/100 \text{ km s}^{-1} \text{ Mpc} = 0.72$, $\sigma_8 = 0.80$, and $n_s = 0.96$. The characteristic collapse mass, M_* , defined as the characteristic mass scale at which the RMS of the linear density field is equal to 1.686 at the present time. For the present simulations, $M_* = 10^{12.5} h^{-1} M_\odot$ at $z = 0$. Outputs of the two simulations are made at 100 snapshots, from $z = 18.4$ to $z = 0$ equally spaced in the logarithm of the expansion factor.

Dark matter halos are identified using a friends-of-friends (FOF) group-finder with a linking length $b = 0.2$ (Davis et al. 1985). We use the SUBFIND algorithm

(Springel et al. 2001) to identify gravitationally bound substructures (subhalos) within each FOF halo. This in turn makes it possible to build up halo merger trees to represent the detailed assembly histories of individual halos. Each member particle of a subhalo is assigned a weight that decreases with the absolute value of its binding energy. For a subhalo ‘A’ in a snapshot, its descendant is identified as the subhalo that is in the subsequent snapshot and contains the largest weighted number of particles belonging to ‘A’, and ‘A’ is considered as the progenitor of its descendant. In each FOF halo, the most massive subhalo is referred to as the main halo, and the branch that traces the main progenitors of the main halo back in time is referred to as the main trunk of the merging tree.

Using the halo merger tree, we can also identify splashback halos (e.g. Ludlow et al. 2009; Wang et al. 2009), which are the main halos at $z = 0$ but have ever been accreted by other massive halos in the past. As shown in Section 3, splashback halos mainly affect the secondary bias for small halos. These halos are expected to have experienced strong non-linear processes, in contrast to other normal halos. Since they are only a small fraction of the total halo population, we do not consider them in most of our analyses.

We select three representative halo samples at $z = 0$ to show our main results. They include 877,692 halos with $11 \leq \log M_h / h^{-1} M_\odot \leq 11.2$ (representing low-mass halos) from the ELUCID simulation, 397,616 halos with $12.4 \leq \log M_h / h^{-1} M_\odot \leq 12.6$ (representing M_* halos) and 9,085 halos with $13.9 \leq \log M_h / h^{-1} M_\odot \leq 14.1$ (representing massive halos) from the S1k simulation. Each of these halos contains more than 300 dark matter particles. As shown in Gao et al. (2005) and Bett et al. (2007), for halos with more than 300 particles, the three halo parameters described in the next subsection can be reliably measured. Our results using ELUCID and S1k, which have very different mass resolutions, shown in Section 3, also support that the mass resolution does not significantly affect our conclusion. We will also show results for other halo mass bins when necessary.

2.2. Halo properties and overdensities

In this paper, we focus on secondary bias of halo distribution using three halo properties: the assembly time, v_{\max}/v_{200} and the spin. Here we list the definitions of these three properties together with halo mass:

- Halo mass M_h : the mass contained in the spherical region of radius r_{200} , centered on the most bound particle of the main halo, where the mean mass density is equal to 200 times the critical density.
- Halo assembly time z_f : the redshift at which M_h reaches half of its final mass at $z = 0$. It is determined by tracing the main trunk of the merger tree of the halo in question.
- v_{\max}/v_{200} : the ratio of the peak value of its circular velocity profile to the virial velocity. Here virial velocity is defined as the circular velocity at r_{200} . This parameter is often used to characterize the concentration of a halo (e.g. Gao & White 2007).
- Halo spin λ : defined as $\lambda = |J|/(\sqrt{2}M_h v_{200} r_{200})$, where J is the angular momentum measured by using particles within a sphere of r_{200} .

As mentioned in the introduction, for a given halo mass, the halo bias depends significantly on the other three halo properties. To avoid ambiguity, we refer to them as the z_f bias, the v_{\max}/v_{200} bias and the λ bias, respectively. To understand their origin, we use over-densities measured on different scales from both the evolved and linear density fields. We thus need to know the positions of the proto-halos that correspond to the halos identified at $z = 0$. For each FOF halo at $z = 0$, the position of the proto-halo is defined as the average position of all particles that end up in the $z = 0$ halo. Here is the list of the over-densities used in our analyses:

- δ_b , the overdensity measured within a large comoving radius range, $R_b = [10 - 15] h^{-1} \text{Mpc}$, centered on each halo at $z = 0$. It is used to infer the halo bias factor at $z = 0$.
- $\delta^i(R)$, the linear overdensity at $z = 18.4$ at a series of comoving radius R , centered on the position of a proto-halo.
- δ_b^i , the linear overdensity at the comoving radius R_b at $z = 18.4$, centered on the position of a proto-halo. Note that δ_b^i is exactly $\delta^i(R)$ when $R = R_b$.
- δ_L^i , the linear overdensity at $z = 18.4$ within the halo Lagrangian radius, R_L , centered on the position of its proto-halo. $R_L \equiv (M_h/(4\pi/3\bar{\rho}))^{1/3}$, where M_h is the halo mass of the corresponding halo at $z = 0$ and $\bar{\rho}$ is the mean comoving density of the universe. Note that δ_L^i is exactly $\delta^i(R)$ when R is chosen in the range of $[0, R_L]$.
- δ_e^i , the linear overdensity at $z = 18.4$ within $(1-1.5)R_L$ for a proto-halo. It is exactly $\delta^i(R)$ when $R = [R_L, 1.5R_L]$.

As shown in Han et al. (2019), the bias factor at the scale from 5 to $20 h^{-1} \text{Mpc}$ is well consistent with the linear theory. We thus adopt $R_b = [10, 15] h^{-1} \text{Mpc}$ to measure δ_b . For any given halo sample, the halo bias is calculated as

$$b_h = \frac{\langle \delta_b \rangle}{\bar{\delta}_{b,p}}, \quad (1)$$

where $\langle \cdot \rangle$ denotes the average over all halos in the sample, and $\bar{\delta}_{b,p}$ is the mean overdensity measured at R_b centered on all particles in the density field at $z = 0$.

The linear densities used in this paper are measured from the snapshot at $z = 18.4$ rather than the initial condition at $z = 100$. At $z = 100$, the true overdensity is very small and shot noise of particles is still important, which can lead to systematical bias in the estimate of the true linear density fluctuations. On the other hand, the overdensities obtained at $z = 18.4$ are in good agreement with the prediction of the linear perturbation theory (see Appendix). Finally, we note that the Lagrangian radii, R_L , for the three representative halo samples are about 0.75, 2.19 and $6.94 h^{-1} \text{Mpc}$, respectively.

3. Halo secondary bias in evolved and linear density fields

Fig. 1 shows the secondary bias for the three halo properties, z_f (left), v_{\max}/v_{200} (middle) and λ (right). In a given narrow mass range (0.2 dex), we select two sub-samples that consist of halos in the lower and upper 20 percent tails of the

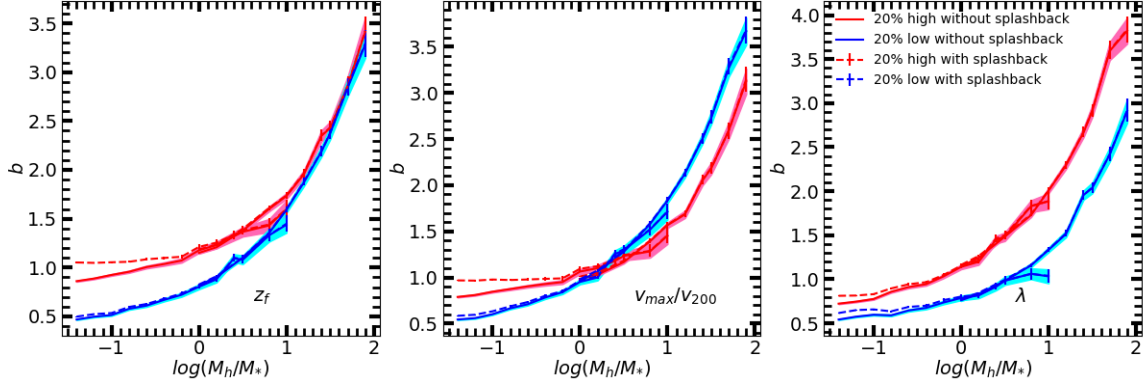


Fig. 1. Halo bias factor as a function of halo mass and halo properties. The red(blue) lines show the results for halos in the upper(lower) 20% tails of the distribution of a given halo property as indicated in each panel. Dashed lines show the results for all halos, while solid lines show the results excluding splashback halos. Simulation ELUCID and S1k are used to calculate the bias in the mass range of $M_h/M_* < 10$ and $M_h/M_* > 1$, respectively. The error bars show the standard deviation calculated by 1000 bootstrap samples.

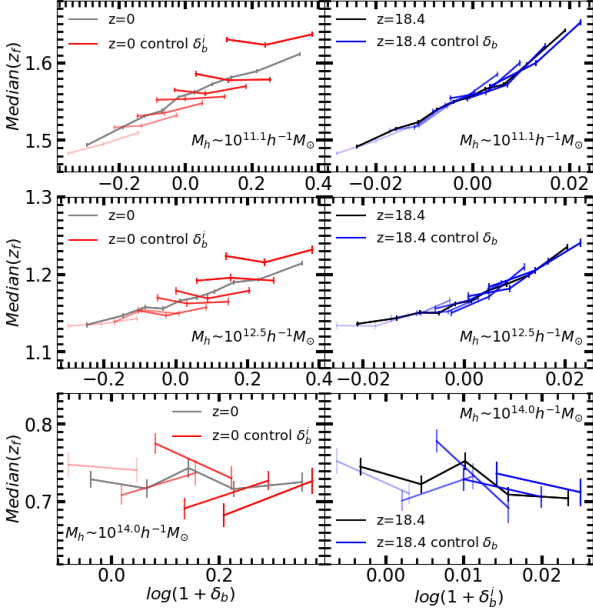


Fig. 2. Median z_f as a function of δ_b and δ_b^i for three representative halo samples as indicated in the panels. The red(blue) lines in left(right) panels show the results with δ_b^i (δ_b) controlled. The error bar shows the standard deviation calculated by 1000 bootstrap samples.

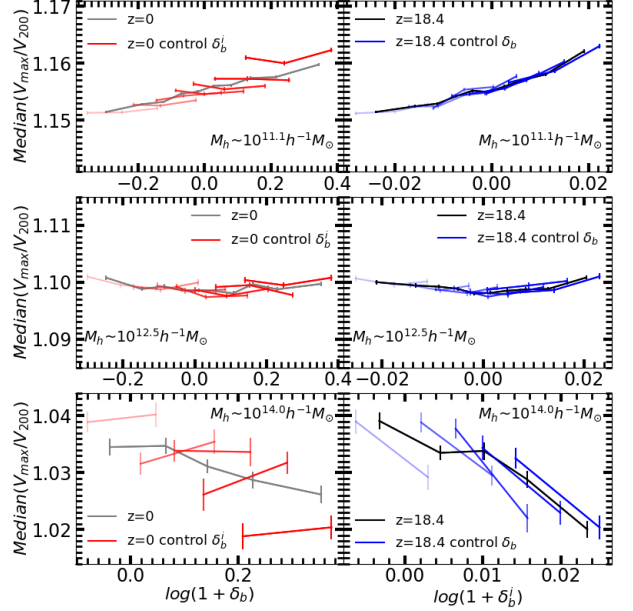


Fig. 3. Similar to Fig. 2 but for v_{\max}/v_{200} .

mass range, suggesting that our results are not significantly affected by numerical resolutions.

Fig. 1 shows that splashback halos mainly affect results for low-mass halos, as expected from the fact that the fraction of the splashback population decreases with increasing halo mass (Wang et al. 2009). The exclusion of splashback halos decreases the bias for halos in the upper percentiles of the z_f and v_{\max}/v_{200} distributions, while the halo bias for the lower percentiles is not affected significantly. This is expected. At low z_f , halo bias depends only weakly on the z_f (see e.g. Gao et al. 2005), while splashback halos on average have higher z_f (e.g. Wang et al. 2009). Splashback halos have a significant impact on the λ bias for halos in both the upper and lower percentiles. Splashback halos are

expected to have experienced strong non-linear evolution, and consequently behave very differently from other halos in their relations with the linear density field. To reduce uncertainties by splashback halos, we exclude them in our analyses.

All the three parameters show strong secondary bias, but with very different halo-mass dependence (see also e.g. [Faltenbacher & White 2010](#); [Salcedo et al. 2018](#)). Older halos are usually more strongly clustered than younger ones of the same mass. However, the z_f bias becomes weaker as halo mass increases and is almost absent at $\log(M_h/M_*) > 1$. The v_{\max}/v_{200} bias is significant over the whole mass range covered. More interestingly, it changes sign around $M_h \sim M_*$, above which less concentrated halos are more strongly biased. The λ bias is also strong in the whole mass range. Different from the other two parameters, its strength increases with the halo mass.

It is known that v_{\max}/v_{200} increases with z_f at given halo mass (e.g. [Gao et al. 2004](#); [Han et al. 2019](#)), and so the z_f bias and v_{\max}/v_{200} bias may have a similar origin for low mass halos, as suggested by previous studies (e.g. [Chen et al. 2020](#)). However, for massive halos, the two secondary biases behave differently from the expectation of the correlation between the two parameters. Moreover, it is also known that older halos tend to have smaller spin in the whole mass range (e.g. [Hahn et al. 2007](#); [Wang et al. 2011](#)), and so the z_f bias and λ bias must have been caused by different processes.

To understand the origin of the secondary bias and the complicated mass dependence shown above, we investigate the correlations of the halo properties with the linear density field. Here we first focus on δ_b^i , which is estimated at the same comoving scale as δ_b . In the next section, we will consider densities defined on other scales. The results, together with comparisons with δ_b , for the three representative halo samples are shown in Figs. 2, 3 and 4. We split each of the representative halo samples into several equal-sized sub-samples according to δ_b or δ_b^i , and calculate the medians of the three halo properties for each sub-sample. We show the bias factors for individual sub-samples of fixed δ_b^i as a function of δ_b in the left panels, and those for fixed δ_b as a function of δ_b^i in the right panels.

For the halo assembly time, one can see clear dependence on both of the two density indicators, δ_b and δ_b^i . The dependence weakens with increasing halo mass and disappears for cluster-sized halos, consistent with the results shown in Fig. 1. The similarity in the results obtained from the two densities is expected, as they are strongly correlated, as shown in Fig. 5. To understand the dependence in more detail, we fix δ_b^i and show the median z_f as a function of δ_b in the left panels, and vice versa in the right panels. For the two low mass bins, the dependence on δ_b becomes very weak when δ_b^i is controlled. On the other hand, when δ_b is controlled, the correlation of z_f with δ_b^i for individual sub-samples follow the overall trend closely. For the most massive halos, no clear trend can be seen.

The results for v_{\max}/v_{200} are also consistent with those shown in Fig. 1. One sees that the correlation shows the opposite trends for low-mass and the most massive halos. The overall trends with δ_b and δ_b^i are similar. However, as shown in Fig. 3, for both low and high mass halos, the dependence on δ_b is absent when δ_b^i is controlled, but a clear correlation (positive for low-mass halos and negative

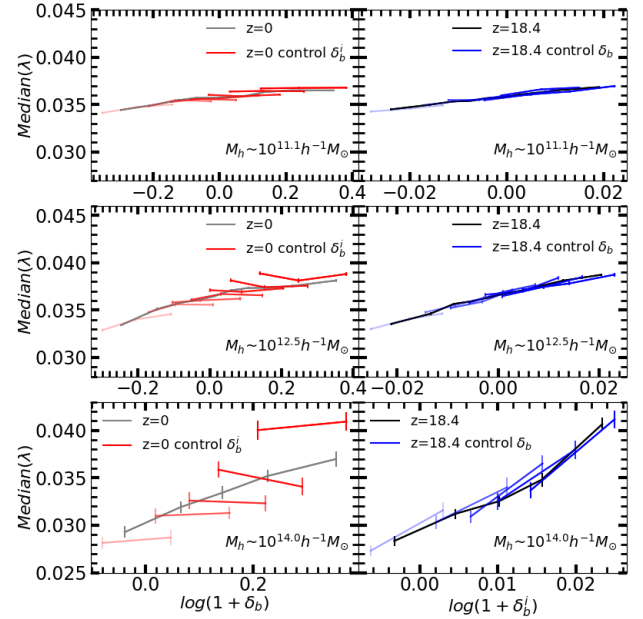


Fig. 4. Similar to Fig. 2 but for spin, λ .

for high-mass halos) is clearly seen with δ_b^i for fixed δ_b . For halos with $M_h \sim M_*$, on the other hand, the trends of v_{\max}/v_{200} with δ_b^i and δ_b are equally weak.

The overall correlation of λ with the two density quantities becomes stronger as the halo mass increases, consistent with the results shown in Fig. 1. If samples are not controlled, the general trend in the λ - δ_b correlation is similar that in the λ - δ_b^i correlation. The results for the controlled samples show clearly that, for all the three halo samples, the linear density, δ_b^i , is the driving factor of the λ bias.

The results presented above suggest that all the three halo properties are correlated with the linear density δ_b^i , in a way similar to the correlation with the evolved density δ_b . Our detailed analyses demonstrate clearly that the correlation with δ_b is driven by the correlation with δ_b^i in all cases where significant secondary bias is detected, through the correlation between δ_b and δ_b^i . This suggests that the understanding of the origin of the secondary bias can be approached by investigating the correlations of halo properties with the linear density field, as we will do below.

4. Correlations of Halo properties with linear densities at various scales

The results presented above show that halo properties are correlated with the linear over-density at a large comoving scale, R_b . [Wang et al. \(2007\)](#) found that halo assembly time is also correlated with the linear over-density measured within the Lagrangian radius, δ_L^i . These two results suggest that halo properties are correlated with the linear density field on various scales. It is thus interesting to first investigate in more detail how the correlation varies with the scale. A convenient way to characterise the correlation strength of two variables, x and y , is to use their Pearson

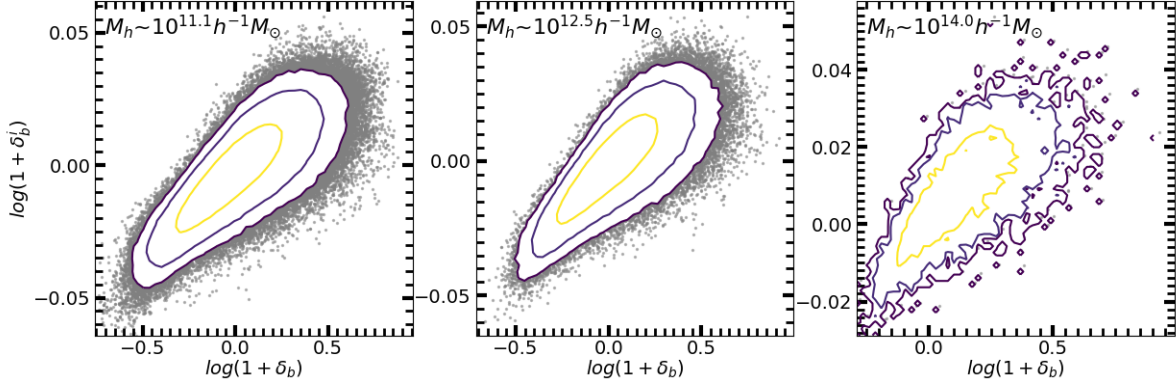


Fig. 5. δ_b^i vs. δ_b for three representative halo samples as indicated in each panel. The three contour lines in each panel enclose 67%, 95% and 99% of halos.

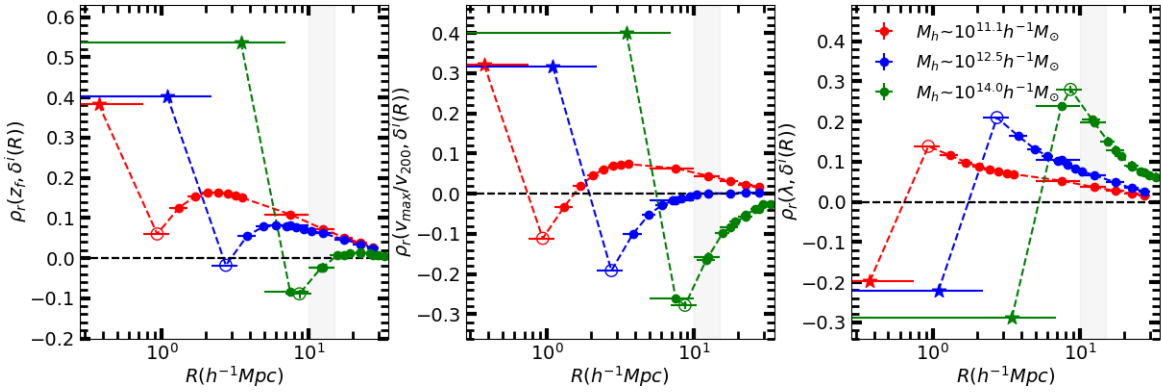


Fig. 6. Pearson correlation coefficients (ρ_r) between halo properties (left panel: z_f , middle panel: v_{\max}/v_{200} and right panel: λ) and $\delta^i(R)$ as a function of R for three representative halo samples as indicated in each panel. The horizontal error bars indicate the R range used to calculate the linear overdensity and the vertical error bars (usually too small to be seen) indicate the uncertainties of the coefficients, calculated using 200 bootstrap samples. The results for δ_L^i and δ_e^i are marked with stars and open circles, respectively. Results on other scales are shown with solid circles. The vertical shaded region indicates the range of R_b used to estimate the halo bias.

correlation coefficient, defined as

$$\rho_r(x, y) = \frac{\langle (x - \bar{x})(y - \bar{y}) \rangle}{\sigma_x \sigma_y}, \quad (2)$$

where \bar{x} (\bar{y}) and σ_x (σ_y) are the mean and standard deviation of the variable x (y). As discussed in Han et al. (2019), the Pearson coefficient is a powerful tool for correlation analysis. If the two variables are roughly linearly correlated, the coefficient measures the steepness of the correlation between the corresponding normalized variables.

The Pearson coefficient, ρ_r , for the correlation of halo properties with $\delta^i(R)$ is shown in Fig. 6. Let us first look at the coefficients at the scale $R = R_b$ (indicated by the vertical bands), i.e. with $\delta^i(R) = \delta_b^i$, and compare them with the results shown in the last section. The absolute values of the correlation coefficients of the three halo properties with δ_b^i range from 0 to 0.2, indicating that the secondary bias is in general a weak effect. The results show that δ_b^i is positively correlated with z_f for the two low-mass samples, and that the coefficient is close to zero for the most massive halos. The coefficient for v_{\max}/v_{200} changes its sign around M_* , being positive and negative for halos of lower

and higher masses, respectively. The correlation coefficient for λ is always positive and increases with halo mass. All of these are in good agreement with the results shown in the last section.

Compared to δ_b^i , δ_L^i is much more strongly correlated with halo properties. In fact, as shown in Fig. 6, δ_L^i almost always has the strongest correlation with the three halo properties. In Fig. 7, the red lines show the coefficients between the three halo properties and δ_L^i as a function of halo mass. As one can see, all the correlations show only a weak dependence on halo mass. The three halo properties have different correlation strengths with δ_L^i , being the strongest for z_f ($\rho_r = 0.4 \rightarrow 0.6$) and the weakest for λ ($\rho_r = -0.2 \rightarrow -0.3$).

Looking at the scale-dependence of these correlations, we see that the dependence is complex, although it is similar for all the three halo properties. There is a quick change in the strength or even in the sign of the correlations at around the Lagrangian radius, R_L , and the correlation coefficients gradually approach to zero at large scales. At $R = (1, 1.5]R_L$, the coefficients reach a (local) minimum for z_f and v_{\max}/v_{200} , and a maximum for λ . The correlation with the over-density at $(1, 1.5]R_L$, i.e. with δ_e^i , shows

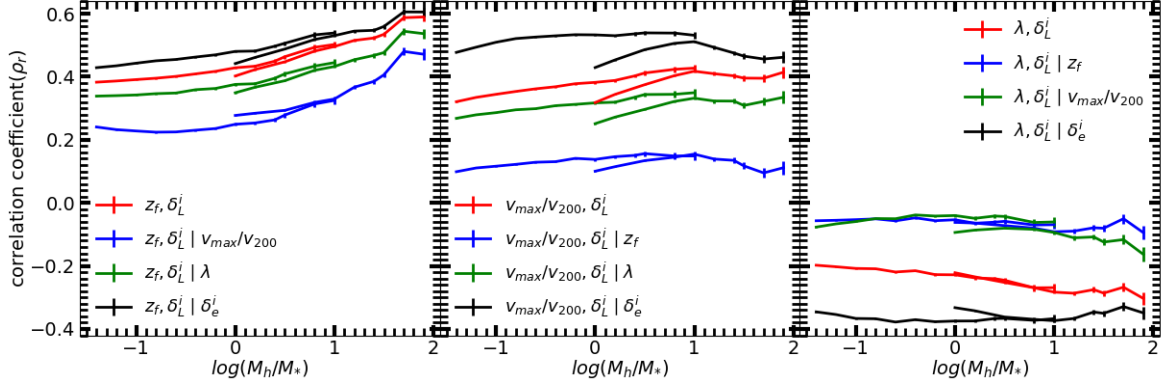


Fig. 7. Pearson coefficients for the (partial) correlations of δ_L^i with halo properties, z_f (left panel), v_{\max}/v_{200} (middle panel) and λ (right panel), as a function of halo mass. As indicated in each panel, the red lines show the results for the correlations between δ_L^i and halo properties, the blue and green lines show the results with another property controlled, and the black lines show the results with δ_e^i controlled. The error bar shows the standard deviation calculated by 200 bootstrap samples.

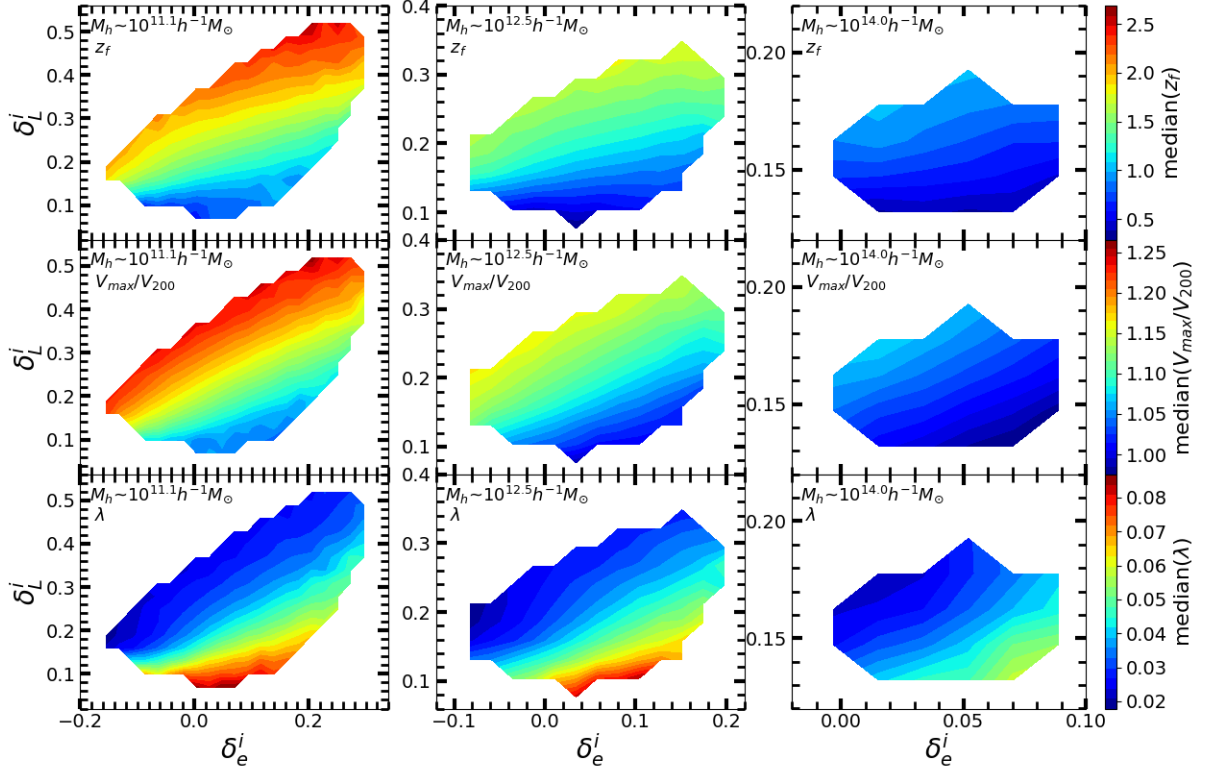


Fig. 8. Contours show Median z_f (upper panels), v_{\max}/v_{200} (middle panels), λ (lower panels) as a function of δ_e^i and δ_L^i for three representative halo samples as indicated in the panels. Only grids containing more than 100 halos are presented.

a complex dependence on halo mass, which is different from the dependence on δ_L^i and δ_e^i . For z_f , the correlation changes its sign around M_* , while for v_{\max}/v_{200} and λ , the correlation strength increases with halo mass.

These curves suggest that both δ_L^i and δ_e^i can affect the halo properties significantly. To better understand the effects, we show in Fig. 8 the halo properties in the (δ_L^i, δ_e^i) space. As one can see, the three halo proper-

ties exhibit strong dependence on both quantities in all the three mass bins. Consistent with the correlation coefficient results shown in Fig. 6, both z_f and v_{\max}/v_{200} have a strong positive correlation with δ_L^i , while λ has a negative correlation with δ_L^i . We also see a clear *negative* correlation of both z_f and v_{\max}/v_{200} , and a clear *positive* correlation of λ , with δ_e^i for given δ_L^i . These signs of correlation are not always consistent with the results shown in Fig. 6. The dis-

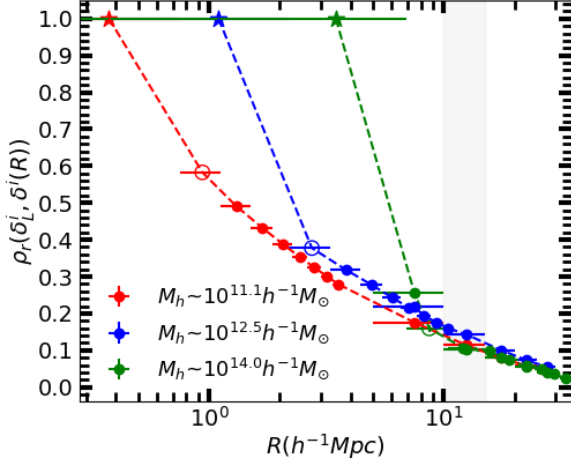


Fig. 9. Pearson coefficients between δ_L^i and $\delta^i(R)$ as a function of R for three representative halo samples. The symbols, color, error bars and shaded region are the same as Fig. 6.

crepancy is produced by the fact that δ_L^i and δ_e^i are correlated, so that the correlation with δ_e^i depends on whether or not δ_L^i is controlled. Fig. 9 shows the correlation coefficient between δ_L^i and $\delta^i(R)$ as a function of R . Clearly, δ_L^i is correlated with the over-density on different scales, including δ_e^i . At given halo mass, the correlation coefficient decreases gradually with R , while at a given $R > R_L$, the correlation strength depends only weakly on halo mass.

It is thus important to disentangle these correlations, and we use partial correlation coefficient to do so. The partial correlation coefficient measures the correlation coefficient between two quantities, x and y , with a third parameter, z , controlled, and is defined as

$$\rho_r(x, y|z) = \frac{\rho_r(x, y) - \rho_r(x, z)\rho_r(y, z)}{\sqrt{1 - \rho_r^2(x, z)}\sqrt{1 - \rho_r^2(y, z)}} \quad (3)$$

(see John et al. 1989). Higher-order partial coefficient can be computed from the lower-order coefficient. For example, when two variables, z and w , are controlled, the coefficient can be written as,

$$\rho_r(x, y|z, w) = \frac{\rho_r(x, y|z) - \rho_r(x, w|z)\rho_r(y, w|z)}{\sqrt{1 - \rho_r^2(x, w|z)}\sqrt{1 - \rho_r^2(y, w|z)}} \quad (4)$$

The correlation coefficients between the three halo properties and δ_L^i , with δ_e^i controlled, are plotted in Fig. 7. With δ_e^i controlled, the correlations with δ_L^i become significantly stronger. This is expected, as the two densities are positively correlated (Fig. 9) but they have opposite correlations with the halo properties (Fig. 8). Note again that the halo mass dependence in these correlations are all weak.

The correlation coefficients between the halo properties and $\delta^i(R)$, with δ_L^i controlled, are shown in Fig. 10. Here results are shown as a function of R/R_L , instead of R . Controlling δ_L^i boosts the correlation strengths between δ_e^i and the halo properties, and makes the coefficients monotonous functions of R/R_L at $R/R_L > 1$. Among the three halo properties, v_{\max}/v_{200} has the strongest (anti-) correlation with δ_e^i , and z_f the weakest. Moreover the positive correlation of λ with $\delta^i(R)$ extends to $R > 5R_L$. In general,

the correlations with δ_e^i and density at larger scales are the opposite to the correlations with δ_L^i , consistent with the results shown in Fig. 8. Remarkably, the correlations with $\delta^i(R)$ at $R > R_L$ depend on halo mass much weaker than seen in Fig. 6. To demonstrate this more clearly, we also show the results for other 13 mass bins, ranging from $10^{11.2}$ to $10^{14.5} h^{-1} M_\odot$, as the gray lines. As one can see, the controlled correlations between halo properties and over-density at $R > R_L$ indeed have weak dependence on halo mass.

These results clearly suggest that two distinct types of processes may regulate the halo properties simultaneously. The first is related to the mean over-density within the proto-halos, i.e. δ_L^i . According to spherical collapse model, the mean linear over-density should be the same for all halos identified at the same time. The fact that δ_L^i is different for different halos indicates that the spherical collapse model is not accurate. As shown in Wang et al. (2007), some halos need a higher over-density to form, because local tidal fields may act to prevent the collapse of the outer parts of proto-halos. This may explain the positive correlations of δ_L^i with z_f and v_{\max}/v_{200} , and the negative correlation with λ . The second is the negative controlled correlation of the over-density at $R > R_L$ with both z_f and v_{\max}/v_{200} , and the positive correlation with λ , when δ_L^i is controlled. As we will see later, these correlations are partly produced by the anti-correlation between the inner density of a proto-halo and the density exterior to R_L . Both types of correlations have only weak dependence on halo mass, presumably because the linear density field is roughly scale-free over the scales concerned here. For convenience, we use L -correlations to refer to those related to δ_L^i , and E -correlations to those related to δ_e^i and over-densities on larger scales.

Since the three halo properties are correlated with each other, it is important to check whether the L - and E - correlations for a specific halo property are induced by the correlations for another halo property. In Fig. 7, we show the correlation coefficients between δ_L^i and one halo property with another property controlled. As z_f is fixed, the correlations with both v_{\max}/v_{200} and λ are largely reduced and close to zero. While v_{\max}/v_{200} or λ is fixed, the correlation with z_f is still strong. It suggests that the z_f - δ_L^i correlation is the dominant one in the L effect, the other two correlations are mainly the secondary effect.

In Fig. 10, we show different partial E -correlation coefficients with z_f or v_{\max}/v_{200} or λ controlled in addition to δ_L^i . We see that the E -correlation for v_{\max}/v_{200} changes little when z_f or λ is controlled. Similarly, halo properties v_{\max}/v_{200} and z_f have only little influence on the E -correlation for λ . However, the E -correlation for z_f is strongly affected by the other two properties, in particular v_{\max}/v_{200} . When v_{\max}/v_{200} is controlled, the E -correlation efficient of z_f becomes close to zero over a large range of scales. These results suggest that the E -correlation of z_f is largely the secondary effect of the E -correlation of v_{\max}/v_{200} , while the E -correlation of λ has a different origin from that of both z_f and v_{\max}/v_{200} .

To gain more understanding of the origin of the E -correlations, we calculate the linear over-density within $2/3R_L$ for each proto-halo, and we denote it by δ_{in}^i . We show the partial correlation between δ_{in}^i and $\delta^i(R)$ with δ_L^i controlled in Fig. 11. As one can see, similar to that of the E -correlations of v_{\max}/v_{200} and z_f . At a given δ_L^i ,

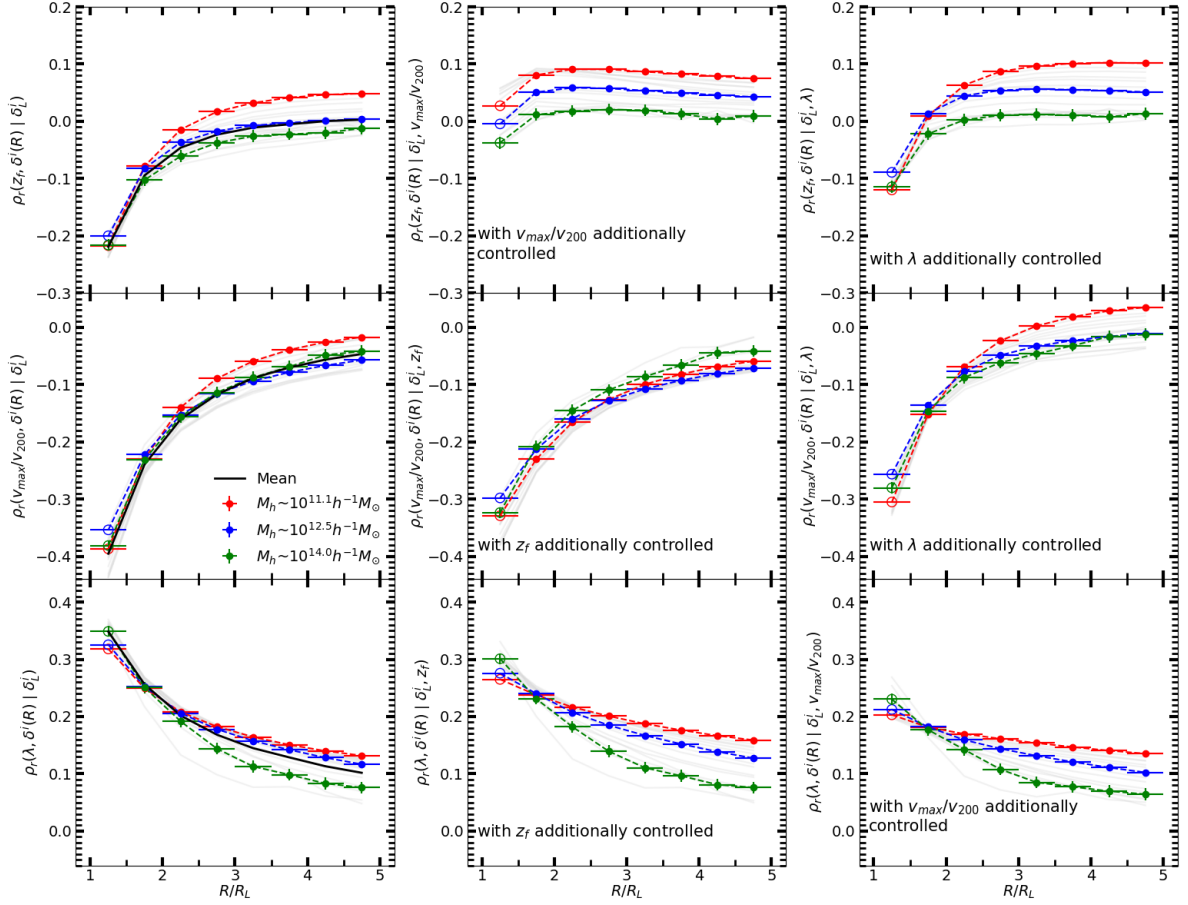


Fig. 10. Partial correlation coefficients for correlations between halo properties and $\delta^i(R)$, with δ_L^i controlled (left panel), with δ_L^i or another halo property additional controlled (middle and right panel), as a function of R/R_L . The results in left panels are computed by using Eq. 3 and those in the middle and right panels using Eq. 4. The symbols, color-code and error bars are the same as Fig. 6. The gray lines show the results for other halo mass bins and the black lines show the mean results over all of these halo mass bins.

δ_{in}^i measures the density slope within the proto-halo. The anti-correlation between δ_{in}^i and the linear density field immediately exterior to R_L indicates that the density slope is coherent over a range of scales around R_L . As suggested in Lu et al. (2006); Dalal et al. (2008), the linear density profile of a proto-halo affects its accretion history and its final properties, such as z_f and v_{max}/v_{200} , which may explain, at least partly, the E -correlations of v_{max}/v_{200} and z_f . The density slope may also affect λ , not only because it is correlated with the moment of inertial tensor of the proto-halo, which couples the proto-halo with the tidal field, but also because of its correlation with the halo assembly time over which the external tidal field operates to generate the angular momentum.

5. On the origin of the secondary bias and its mass dependence

From Eq. 3, we can derive the Pearson coefficient between a halo property, p , and δ_b^i as,

$$\rho_r(p, \delta_b^i) = \alpha \rho_r(p, \delta^i(r_b) | \delta_L^i) + \rho_r(p, \delta_L^i) \rho_r(\delta_b^i, \delta_L^i) \quad (5)$$

where $r_b = R_b/R_L$, $\delta^i(r_b)$ is exactly δ_b^i , and

$$\alpha = \sqrt{(1 - \rho_r^2(p, \delta_L^i))(1 - \rho_r^2(\delta_b^i, \delta_L^i))} \quad (6)$$

Since $\rho_r(p, \delta_L^i)$ ranges from ~ -0.3 to ~ 0.6 and $\rho_r(\delta_b^i, \delta_L^i)$ is about 0.1, the value of α ranges from 0.8 to 1, with very weak dependence on halo mass. We thus can treat α as a constant close to unity.

Eq. 5 shows that the correlation of halo properties with δ_b^i consists of two components, represented by the two terms on the right-hand side and related to the L - and E -correlations, respectively. The secondary bias in the evolved

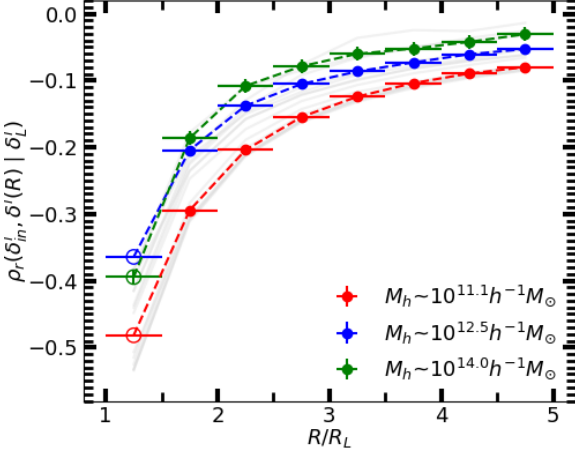


Fig. 11. Partial correlation coefficients (Eq. 3) for correlations between δ_m^i and $\delta^i(R)$, with δ_L^i controlled, as a function of R/R_L . δ_m^i is the linear overdensity within $2/3 R_L$. The symbols, color-code and error bars are the same as Fig. 10.

space, which is usually characterized by the p - δ_b correlation, can thus be understood in terms of the p - δ_b^i correlation, as δ_b^i is tightly correlated with δ_b and the correlation is quite independent of halo mass (Fig. 5). The E -correlation can result in a negative correlation of δ_b^i with z_f and v_{\max}/v_{200} and a positive correlation with λ . The L -correlation impacts the secondary bias via the δ_L^i - δ_b^i correlation, and can induce a positive correlation of δ_b^i with z_f and v_{\max}/v_{200} and a negative correlation with λ . As shown in Figs. 7 and 10, both components depend weakly on halo mass. However, as we will show below, the two components together can actually produce the mass dependence observed in the secondary bias.

Let us first look at the z_f bias. For small halos with $\log(M_h/h^{-1}M_\odot) = 11.1$, the radius R_b corresponds to $r_b = R_b/R_L > 13.4$. At such a large scaled radius, the E -correlation is very weak, with $\rho_r(z_f, \delta^i(r_b) | \delta_L^i)$ close to zero (Fig. 10). In this case, $\rho_r(z_f, \delta_b^i) \simeq \rho_r(z_f, \delta_L^i) \rho_r(\delta_b^i, \delta_L^i)$, indicating that the positive correlation of z_f with δ_b^i for these halos is mainly determined by the L -correlation. For M_* halos, where $r_b = [4.56, 6.84]$, the contribution from E -correlation is still negligible, and so the dominant role is still played by the L -correlation. Moreover, since the z_f - δ_L^i and δ_b^i - δ_L^i correlations for M_* halos are similar to those for small halos (Fig. 6 and 9), the contribution of the L -correlation for the two halo mass samples are also similar. Indeed, as shown in Fig. 6, the correlation coefficients of z_f with δ_b^i are very similar for the two halo samples. Finally, for massive cluster-sized halos, the scaled radius $r_b = [1.44, 2.16]$. At such a scale, the E -correlation becomes much stronger (Fig. 10), while the contribution of the L -correlation is only slightly stronger than that for the other two halo mass bins. Consequently, the E -correlation is able to counterbalance the L -correlation, making the secondary bias for these halos very weak.

Similar analysis can also be applied to v_{\max}/v_{200} . The L -correlation of v_{\max}/v_{200} is weaker than that of z_f , while the E -correlation is stronger for v_{\max}/v_{200} than for z_f , making the E -correlation more important for the v_{\max}/v_{200}

bias. This also makes the mass-dependence of the v_{\max}/v_{200} bias different from that of the z_f bias. For small halos, the v_{\max}/v_{200} bias is still dominated by the L -correlation, because $\rho_r(v_{\max}/v_{200}, \delta^i(r_b) | \delta_L^i)$ is close to zero for these halos (Fig. 10). Thus, a positive v_{\max}/v_{200} - δ_b^i correlation is expected, consistent with the results shown in Figs. 1 and 3. For M_* halos, L - and E -correlations become comparable, so that v_{\max}/v_{200} is independent of δ_b^i . For massive cluster-sized halos, where r_b becomes small, the E -correlation becomes the dominant one, producing a negative correlation between v_{\max}/v_{200} and δ_b^i . The reverse of the v_{\max}/v_{200} bias is the result of the competition between the two correlations.

Finally for the spin, the L -correlation is even weaker, and thus plays only a minor role in producing the λ bias. As shown in Fig. 10, the E -correlation for the spin decreases with R/R_L slowly, and so the dominant effect for the λ bias is always the E -correlation across the entire mass range. Since $r_b = R_b/R_L$ decreases with increasing halo mass and the E -correlation is stronger at smaller r_b , we expect an increasing trend with halo mass, as shown in Figs. 1, 4 and 6.

Our analyses clearly show that the z_f , v_{\max}/v_{200} and λ bias can be produced by the L - and E - correlations. The mass dependence of the secondary bias is the result of the competition between the two correlations that depend on $r_b = R_b/R_L$ in different ways. Our results are not sensitive to the choice of R_b , on which the halo bias is estimated. In fact, we reached similar conclusions using other scales, although some details may be different. However, both the E - and L -correlations have some weak but complicated dependence on halo mass, which may also contribute to the secondary bias and their mass dependence. In addition, the correlations of the halo properties with δ_b^i are not expected to be exactly the same as those with δ_b , estimated at $z = 0$, although these two overdensities are correlated. As shown in Figs. 2, 3 and 4, the non-linear evolution of the density field around halos weakens the overall secondary bias slightly. Despite of those, our results demonstrate clearly how the E - and L -correlations in the linear density field are combined to produce the secondary bias.

6. Summary and discussion

In this paper, we use two N -body simulations, ELUCID and S1k, to study the origin of the secondary bias for halo assembly time (z_f), concentration (v_{\max}/v_{200}) and spin (λ), and its dependence on halo mass. Splashback halos, which have experienced strong non-linear processes, are excluded from our analyses. We investigate the correlations of these halo properties with linear densities at various scales in details. Our main results can be summarized as follows.

- We find that the correlations of halo properties with the density measured at $R_b = [10, 15] h^{-1} \text{Mpc}$ are stronger in the linear density field than in the evolved density field at $z = 0$. For most halos, the correlation with the $z = 0$ density is the secondary effect of the correlation with the linear density (Figs. 2, 3 and 4) through the correlation of the two densities (Fig. 5).
- We find strong correlations between the three halo properties and the average linear density within the Lagrangian radius, δ_L^i (Fig. 7). The z_f and v_{\max}/v_{200} of

halos increase with δ_L^i , while λ exhibits a negative correlation with δ_L^i . The Pearson correlation coefficient shows that all the three correlations depend only weakly on halo mass (Fig. 7). Our results suggest that the L -correlations of v_{\max}/v_{200} and λ are the secondary effects of the L -correlation of z_f .

- At a given δ_L^i , all the three halo properties are correlated with $\delta^i(R/R_L)$ at $R > R_L$ in a way opposite to the L -correlation (Figs. 8 and 10). The conditional correlations, with δ_L^i fixed, show only weak dependence on halo mass for all the three halo properties. The E -correlations for z_f and v_{\max}/v_{200} may share the same origin that may be partly related to the correlation of inner slope of proto-halos with large-scale densities. However, the E -correlation of λ may have a different origin.
- For the z_f bias, the L -correlation dominates for almost the whole range of the halo mass, and the contribution of the two correlations are comparable for massive cluster-sized halos. For the v_{\max}/v_{200} bias, the L -correlation dominates for low-mass halos and the E -correlation dominates for massive cluster-sized halos, while the two correlations are comparable for M_* halos. For the λ bias, the E -correlation dominates over the whole mass range and the L -correlation only plays a minor role.
- The L - and E -correlations are the main driving factors of the secondary bias (Eq. 5). The mass dependence of the three secondary bias is the result of the competition of the two correlations and the mass-dependent contribution of the E -correlation.

To fully understand the origin of the secondary bias for the three halo properties, we need to know what mechanisms produce the L - and E -correlations. The L -correlation of z_f has been studied in Wang et al. (2007), who found that the proto-halo of a $z = 0$ halo with high z_f is usually located in the vicinity of massive structures. They thus suggested that the large-scale tidal field associated with the high density can truncate the accretion of the material in the outskirts of the proto-halo. The stronger the tidal field is, the larger the truncation effect and the higher the assembly redshift. This can explain the z_f - δ_L^i correlation. However, they suggested that this effect is only important for small halos (see also e.g. Dalal et al. 2008; Mansfield & Kravtsov 2020), which is not consistent with our results that this effect is equally important for cluster-sized halos. This indicates that the tidal truncation may also be important for massive halos.

The E -correlation can produce a secondary bias effect that is totally opposite to the L -correlation. The E -correlation is complicated and more than one mechanisms may be relevant. For example, previous studies (e.g. Fakhouri & Ma 2009; Wang et al. 2011) suggested that dense environments can enhance the frequency of halo merging, and mass accretion, producing an effect similar to that of the E -correlation we observe. The inner density profile within a proto-halo, which is found to correlate with large-scale density (Fig. 11), can also affect the assembly history and concentration of the halo (e.g. Lu et al. 2006; Dalal et al. 2008). A steeper initial profile in general produces an older and a more concentrated final halo, leading to the E -correlation. External tidal field can not only truncate mass accretion onto a halo but can also accelerate the tangential velocity of the material around the halo and enhance the spin (e.g. Shi et al. 2015). This may explain the

significant positive correlation between the spin and linear density at large scales. The steepness of the initial density profile, which is correlated with the large-scale density field, can also affect the spin through its correlation with the moment of inertial tensor of the proto-halo and its correlation with the assembly time over which the external tidal field operates to generate the angular momentum.

Further investigations are still needed to understand the details of these mechanisms and how they affect the properties of halos. A detailed understanding of these mechanisms is essential not only for understanding the origin of the secondary bias, but also for constructing a comprehensive picture of halo formation in the cosmic density field. We will investigate some of these questions in details in a forthcoming paper.

Acknowledgments

This work is supported by the National Key R&D Program of China (grant No. 2018YFA0404503), the National Natural Science Foundation of China (NSFC, Nos. 11733004, 11890693, and 11421303), and the Fundamental Research Funds for the Central Universities. The work is also supported by the Supercomputer Center of University of Science and Technology of China.

References

- Allgood, B., Flores, R. A., Primack, J. R., et al. 2006, MNRAS, 367, 1781
- Bett, P., Eke, V., Frenk, C. S., et al. 2007, MNRAS, 376, 215
- Chen, S., Wang, H., Mo, H. J., & Shi, J. 2016, ApJ, 825, 49
- Chen, Y., Mo, H. J., Li, C., et al. 2020, ApJ, 899, 81
- Chue, C. Y. R., Dalal, N., & White, M. 2018, JCAP, 2018, 012
- Dalal, N., White, M., Bond, J. R., & Shirokov, A. 2008, ApJ, 687, 12
- Davis, M., Efstathiou, G., Frenk, C. S., & White, S. D. M. 1985, ApJ, 292, 371
- Desjacques, V. 2008, MNRAS, 388, 638
- Dunkley, J., Komatsu, E., Nolte, M. R., et al. 2009, ApJS, 180, 306
- Fakhouri, O. & Ma, C.-P. 2009, MNRAS, 394, 1825
- Faltenbacher, A. & White, S. D. M. 2010, ApJ, 708, 469
- Gao, L., Springel, V., & White, S. D. M. 2005, MNRAS, 363, L66
- Gao, L. & White, S. D. M. 2007, MNRAS, 377, L5
- Gao, L., White, S. D. M., Jenkins, A., Stoehr, F., & Springel, V. 2004, MNRAS, 355, 819
- Hahn, O., Porciani, C., Carollo, C. M., & Dekel, A. 2007, MNRAS, 375, 489
- Hahn, O., Porciani, C., Dekel, A., & Carollo, C. M. 2009, MNRAS, 398, 1742
- Han, J., Li, Y., Jing, Y., et al. 2019, MNRAS, 482, 1900
- Hearin, A. P., Watson, D. F., & van den Bosch, F. C. 2015, MNRAS, 452, 1958
- Jing, Y. P. & Suto, Y. 2002, ApJ, 574, 538
- Jing, Y. P., Suto, Y., & Mo, H. J. 2007, ApJ, 657, 664
- John, N., William, W., & Whitmore, G. A. 1989
- Johnson, J. W., Maller, A. H., Berlind, A. A., Sinha, M., & Holley-Bockelmann, J. K. 2019, MNRAS, 486, 1156
- Lacerna, I. & Padilla, N. 2011, MNRAS, 412, 1283
- Lazeyras, T., Musso, M., & Schmidt, F. 2017, JCAP, 2017, 059
- Li, R., Gao, L., Xie, L., & Guo, Q. 2013, MNRAS, 435, 3592
- Li, Y., Mo, H. J., & Gao, L. 2008, MNRAS, 389, 1419
- Lu, Y., Mo, H. J., Katz, N., & Weinberg, M. D. 2006, MNRAS, 368, 1931
- Ludlow, A. D., Navarro, J. F., Springel, V., et al. 2009, ApJ, 692, 931
- Mansfield, P. & Kravtsov, A. V. 2020, MNRAS, 493, 4763
- Mao, Y.-Y., Zentner, A. R., & Wechsler, R. H. 2018, MNRAS, 474, 5143
- Mo, H. J. & White, S. D. M. 1996, MNRAS, 282, 347
- Musso, M. & Sheth, R. K. 2012, MNRAS, 423, L102
- Paranjape, A., Hahn, O., & Sheth, R. K. 2018, MNRAS, 476, 3631
- Ramakrishnan, S., Paranjape, A., Hahn, O., & Sheth, R. K. 2019, MNRAS, 489, 2977

- Salcedo, A. N., Maller, A. H., Berlind, A. A., et al. 2018, MNRAS, 475, 4411
- Salcedo, A. N., Zu, Y., Zhang, Y., et al. 2020, arXiv e-prints, arXiv:2010.04176
- Sandvik, H. B., Möller, O., Lee, J., & White, S. D. M. 2007, MNRAS, 377, 234
- Sheth, R. K., Mo, H. J., & Tormen, G. 2001, MNRAS, 323, 1
- Shi, J. & Sheth, R. K. 2018, MNRAS, 473, 2486
- Shi, J., Wang, H., & Mo, H. J. 2015, ApJ, 807, 37
- Springel, V. 2005, MNRAS, 364, 1105
- Springel, V., White, S. D. M., Tormen, G., & Kauffmann, G. 2001, MNRAS, 328, 726
- Tucci, B., Montero-Dorta, A. D., Abramo, L. R., Sato-Polito, G., & Artale, M. C. 2020, arXiv e-prints, arXiv:2007.10366
- Wang, H., Mo, H. J., Chen, S., et al. 2018, ApJ, 852, 31
- Wang, H., Mo, H. J., & Jing, Y. P. 2009, MNRAS, 396, 2249
- Wang, H., Mo, H. J., Jing, Y. P., Yang, X., & Wang, Y. 2011, MNRAS, 413, 1973
- Wang, H., Mo, H. J., Yang, X., et al. 2016, ApJ, 831, 164
- Wang, H. Y., Mo, H. J., & Jing, Y. P. 2007, MNRAS, 375, 633
- Wang, P. & Kang, X. 2018, MNRAS, 473, 1562
- Wechsler, R. H. & Tinker, J. L. 2018, ARA&A, 56, 435
- Wechsler, R. H., Zentner, A. R., Bullock, J. S., Kravtsov, A. V., & Allgood, B. 2006, ApJ, 652, 71
- Wetzel, A. R., Cohn, J. D., White, M., Holz, D. E., & Warren, M. S. 2007, ApJ, 656, 139
- Xu, X. & Zheng, Z. 2018, MNRAS, 479, 1579
- Yang, X., Mo, H. J., & van den Bosch, F. C. 2006, ApJ, 638, L55
- Yang, X., Zhang, Y., Lu, T., et al. 2017, ApJ, 848, 60
- Zel'Dovich, Y. B. 1970, A&A, 500, 13
- Zentner, A. R. 2007, International Journal of Modern Physics D, 16, 763
- Zentner, A. R., Hearin, A. P., & van den Bosch, F. C. 2014, MNRAS, 443, 3044
- Zhao, D. H., Jing, Y. P., Mo, H. J., & Börner, G. 2003, ApJ, 597, L9
- Zhu, G., Zheng, Z., Lin, W. P., et al. 2006, ApJ, 639, L5

We use the simulation snapshot at $z = 18.4$, rather than the initial condition (at $z = 100$), to calculate the linear overdensities. When the mass resolution is not sufficiently high, there exists a systematical problem in the linear density field on small scale based in the initial conditions due to shot noise. Fig. 1 shows δ_L^i measured at $z = 18.4$ versus that at $z = 100$ for M_* halos, together with the prediction of the linear theory. As one can see, for ELUCID, where the mass resolution is higher, the correlation is very tight and well consistent with the theoretical prediction. However, for S1k the correlation is much looser. In particular, some discontinuous features are presented at $\delta_L^i(z = 100) \sim 0$. The problem can also be seen in the probability distribution of $\delta_L^i(z = 100)$ for the two simulations (right panel of Fig. 2). A clear discrepancy between the two simulations can be seen at $z = 100$.

As shown in the right panel of Fig. 1, the density correlation between the two redshifts are consistent with the prediction of the linear perturbation theory, indicating that the density field at $z = 18.4$ is still in the linear regime for ELUCID. In the left panel of Fig. 2, we show the probability distribution of $\delta_L^i(z = 18.4)$ for M_* halos from the two simulations. The two distributions are very similar, indicating that the density at $z = 18.4$ measured from S1k is reliable. These results justify the use of the simulation data at $z = 18.4$ to estimate the linear densities.

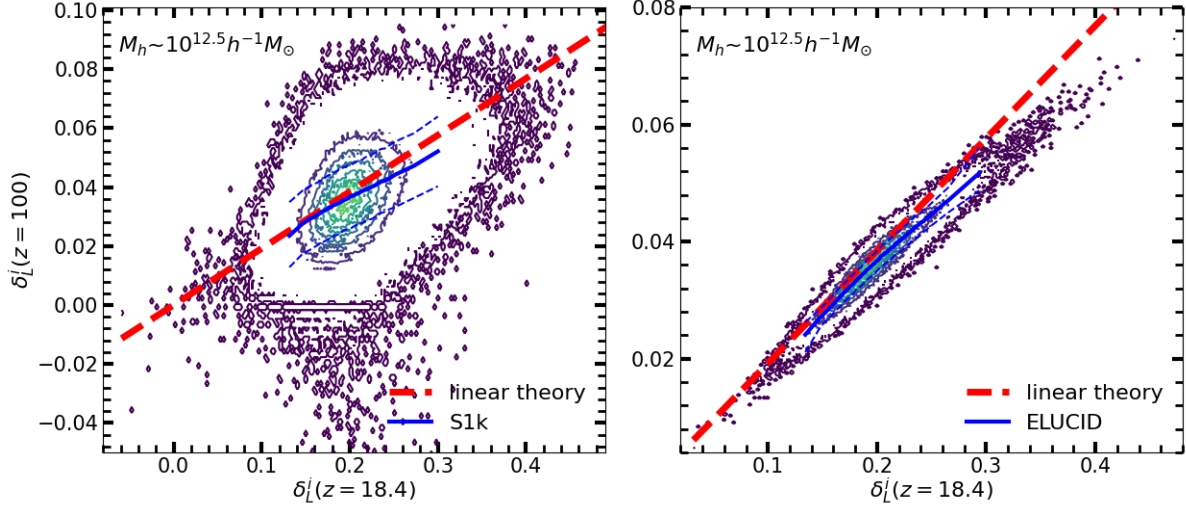


Fig. .1. The correlation between $\delta_L^i(z = 100)$ and $\delta_L^i(z = 18.4)$ for M_* halos. The red dash lines show the prediction of the linear theory. The blue solid line show the median value and the blue dash lines mark the 68 percent confidence intervals. The left (right) panel shows the results for the S1k (ELUCID) simulation.

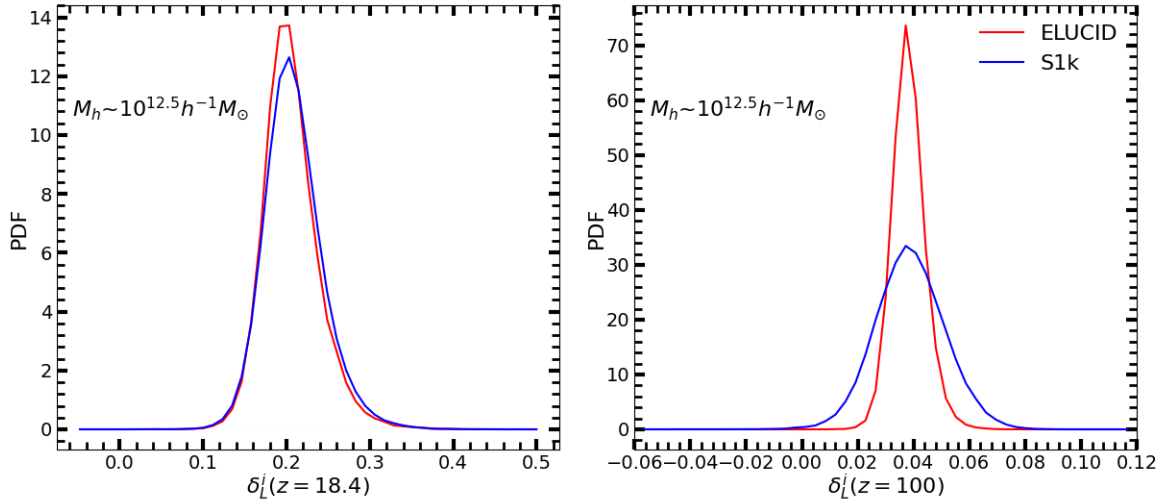


Fig. .2. The probability distributions of $\delta_L^i(z = 18.4)$ (left panel) and $\delta_L^i(z = 100)$ (right panel). The red (blue) lines show the results from the ELUCID (S1k) simulation.